Heteroatom-Substituted Re-Flashed Graphene

Phelecia Scotland,[1,2#] Lucas Eddy,[2,3#] Jinhang Chen,[2] Weiyin Chen,[2] Jacob L. Beckham,[2] Chi Hun Choi,[1,2] Paul Andrade Advincula,[2] Kevin M. Wyss,[2] Paul E. Savas,[2] Lorenzo Castelli,[6] Alexander Lathem,[2,3] Obinna E. Onah,[2,3] Geoff Wehmeyer,[6] Yimo Han,[1] James M. Tour,[1,2,3,4,5*]

[1]Department of Materials Science and NanoEngineering, [2]Department of Chemistry, [3]Applied Physics Graduate Program and Smalley-Curl Institute, [4]NanoCarbon Center and the Rice Advanced Materials Institute, and [5]Department of Computer Science, Rice University, [6]Department of Mechanical Engineering, 6100 Main Street, Houston, Texas 77005, USA

#These authors contributed equally to this work.

*Corresponding Author (Email: tour@rice.edu)

Abstract Flash Joule heating is an ultrafast, energy-efficient, and scalable technique used in the production of a variety of organic and inorganic compounds, including flash graphene. This technique has also been used in the production of doped graphene by flash Joule heating amorphous carbon in the presence of heteroatom-donating compounds. Herein, we report a modified flash Joule heating technique by which graphene is formed with up to 21 at% of the graphene lattice containing substituted heteroatoms. This is achieved by re-flashing graphene in the presence of heteroatom-donating compounds, allowing this substitution to occur at lower temperatures than previously reported for flash Joule heating-synthesized doped graphene and thereby permitting much higher amounts of heteroatom insertion into the graphene lattice. We demonstrate nitrogen, sulfur, phosphorus, and fluorine atom atomic substitution into or upon the graphene lattice, as well as multi-heteroatom substitution. Finally, the implementation of the

nitrogen-substituted re-flashed graphene into battery anodes exhibits improved performance and stability relative to unsubstituted re-flashed graphene battery anodes.

Key words: graphene, flash Joule heating, doped graphene, re-flashed graphene

1. Introduction

Graphene is a two-dimensional material that exhibits extraordinary properties including high electrical conductivity, thermal conductivity, mechanical strength, and diverse optical properties.[1–4] The properties of graphene are further tunable through the modification of its structure and atomic composition.[5–7] Heteroatom substitution is one of the most facile methods of achieving modification of the physical and chemical properties of a material.[8–10] Non-carbon heteroatoms, such as nitrogen, boron, fluorine, and sulfur, which exhibit atomic radii comparable to carbon, are frequently introduced as dopants into the graphene lattice.[8,11,12] The heteroatoms result in modification of the physical and electrochemical properties of graphene, facilitating its use in many applications. The heteroatom functionalization of graphene is commonly achieved through two main approaches: *in situ* (one-step), where graphene synthesis and heteroatom doping are achieved simultaneously; and post-treatment (two-step), where pre-formed graphene or graphene oxide is used as a precursor. Common *in situ* doping strategies include processes such as chemical vapor deposition,[13] and solvothermal methods.[14] These processes sometimes take hours or days, and the solvothermal methods use large quantities of solvents. Post-treatment processes include ball milling,[15] thermal annealing,[16] plasma and laser-induced methods.[17] Sometimes, these processes suffer from localization of the dopants on the edges or defects, destruction of the sp^2 network of the graphene lattice, introduction of impurities, and utilization of

harsh oxidants of the precursors such as graphene oxide (GO).

Here we explore the use of flash Joule heating (FJH) as an alternative technique to rapidly produce various types of high-quality heteroatom doped or substituted flash graphene (FG) (Figure S1). FJH is a method in which an electric current flows through a material, quickly heating it to high temperatures at 10^2 to 10^5 ºC/s within a few milliseconds to seconds range to trigger a chemical reaction. This technique uses the feedstock material as the heating medium, offering a rapid and efficient form of direct heating. The strong local electric fields within the material can heavily polarize the atoms, converting them into open-shell systems that experience swift chemical rearrangements and changes in hybridization.[18,19] FJH has been used in the facile, large-scale synthesis of turbostratic graphene,[18] metastable,[20] phase controlled,[21,22] and doped materials, including doped FG.[8,23]

Recently, we demonstrated that doped FG could be synthesized using FJH in a catalyst-free and solvent-free, approach by adding heteroatom containing materials to the starting carbon source such as carbon black or coke.[8] After FJH to ~3000 °C heteroatom containing FG was afforded. The boiling point of the heteroatom-containing compounds ranges from 50 to 400 °C (Figure S2) and are likely to be distilled out of the system, thus a pressurized tube and sealed system is required to achieve doping. Furthermore, lower mass loadings (25 - 80 mg) were previously used to achieve high levels of heteroatom doping and homogeneity, since previous attempts at scaled-up reactions resulted in decreases in heteroatom concentration and homogeneity.

In this study we demonstrate that by using already formed FG as the feedstock with the addition of the heteroatom material and then re-flashed at lower temperatures, effective heteroatom substitution can be achieved. This uses FJH reaction tubes that are neither fully sealed nor

subjected to pressurization (Figure 1a). This simplifies the cost of equipment and facilitates scaled-up synthesis. Inexpensive and readily available carbon feedstocks, including bituminous activated charcoal (BAC) and metallurgical coke (MC), can be first converted into FG by conventional FJH.[24] Then, they are mixed with the heteroatom-containing material and re-flashed to produce heteroatom-substituted re-flashed graphene (X-rFG) where X can represent B, N, P, S, or F. Since the presence of some of these heteroatoms can exceed 10 at%, they are more accurately described as heteroatom-substituted rather than heteroatom doped. Furthermore, high heteroatom content up to 21 at% is demonstrated. This process is catalyst free, solvent free, solid state, is scalable, and affords up to 3 g of heteroatom-substituted graphene in a single batch. Furthermore, it requires lower operating temperatures for the re-flash (~2000 °C) and is conducted in a non-airtight fused quartz tube, reducing pressure due to the absence of full sealing. We then compare N-re-flashed bituminous activated charcoal FG (N-rBACFG), and rBACFG (without heteroatoms) as an anode material in a half cell of lithium-ion batteries. We demonstrate that substituting nitrogen into BACFG significantly improves the stability over 500 cycles because of an improvement in the Li^+ diffusion coefficient, and a smaller difference in the increase of the resistance during the charge-discharge process.

2. Results and Discussion:

Heteroatom-substituted re-flashed graphene is synthesized by initially subjecting amorphous carbon feedstocks, specifically BAC (Figure S3) and MC,[24,25] to FJH. Several identical FJH reactions of amorphous carbon were performed to produce a standardized master batch of ~30 g of FG. This master batch was then used as the precursor feedstock to ensure sample consistency. Characterization for the BACFG can be found in Figure S4. The heteroatom-containing

compounds used were melamine formaldehyde resin for nitrogen substitution, boric acid for boron substitution, 1,1,1,2,2,3,3,4,4,5,5,6,6,7,7,8,8-heptadecafluoro-10-iododecane or perfluoro sulfonic acid (PFOS) for fluorine substitution; polyphenylene sulfide (PPS) for sulfur substitution; and red phosphorus for phosphorus substitution. The FG powder was then mixed with the heteroatom compounds in ratios shown in Table S1. The powders were ground finely together, using a mortar and pestle, until the final powder had a consistent color and texture. 0.2 g of the powder was added to an 8 mm inner diameter fused quartz tube with graphite cylinders, referred to as spacers, on both ends to cap the cylinder. A stainless-steel spring was placed around the outside of the tube. The reaction vessel holder was placed into a vacuum desiccator that was fitted with cables to connect to the FJH system. Additional information about this setup is found in Section 1 of the Supporting Information.

The loaded reaction vessel was subjected to FJH as shown in (Figure 1a) under argon atmosphere, using the same pulse width modulation-mediated FJH system previously reported.[3] FJH occurs on the millisecond to second time scale (Figure 1b) and the pulse width modulation of the 6.5 s flash discharge aids in flash uniformity. The samples were flashed at voltages ranging from 80 to 100 V. However, a lower voltage of 45-55 V was often used as a pretreatment flash to first melt or degrade the heteroatom source. The maximum temperature of this pretreatment can range between ~340 to ~420 ºC (Figure S5), which aligns with the melting point or decomposition temperature of most heteroatom sources used in these experiments. This process allows the heteroatom source to better wet the carbon feedstock, resulting in a more uniform dispersion of heteroatoms within the graphene lattice. Decomposing the heteroatom source also slightly reduces the electrical resistance of the reactant mixture, reducing the voltage required for the primary flash reaction. Figure 1c shows an example of the current and temperature profiles of the FJH reaction

to synthesize of P-rBACFG at 100 V. The heteroatom substitution percentages of rBACFG and the mass yields of the product after the reaction are shown in Figure 1d and Figure 1e, respectively. The mass yield is obtained by the following Equation 1:

$$\%Mass\ yield = \frac{Mass\ of\ product\ recovered}{Mass\ of\ reactant} \times 100\% \quad (1)$$

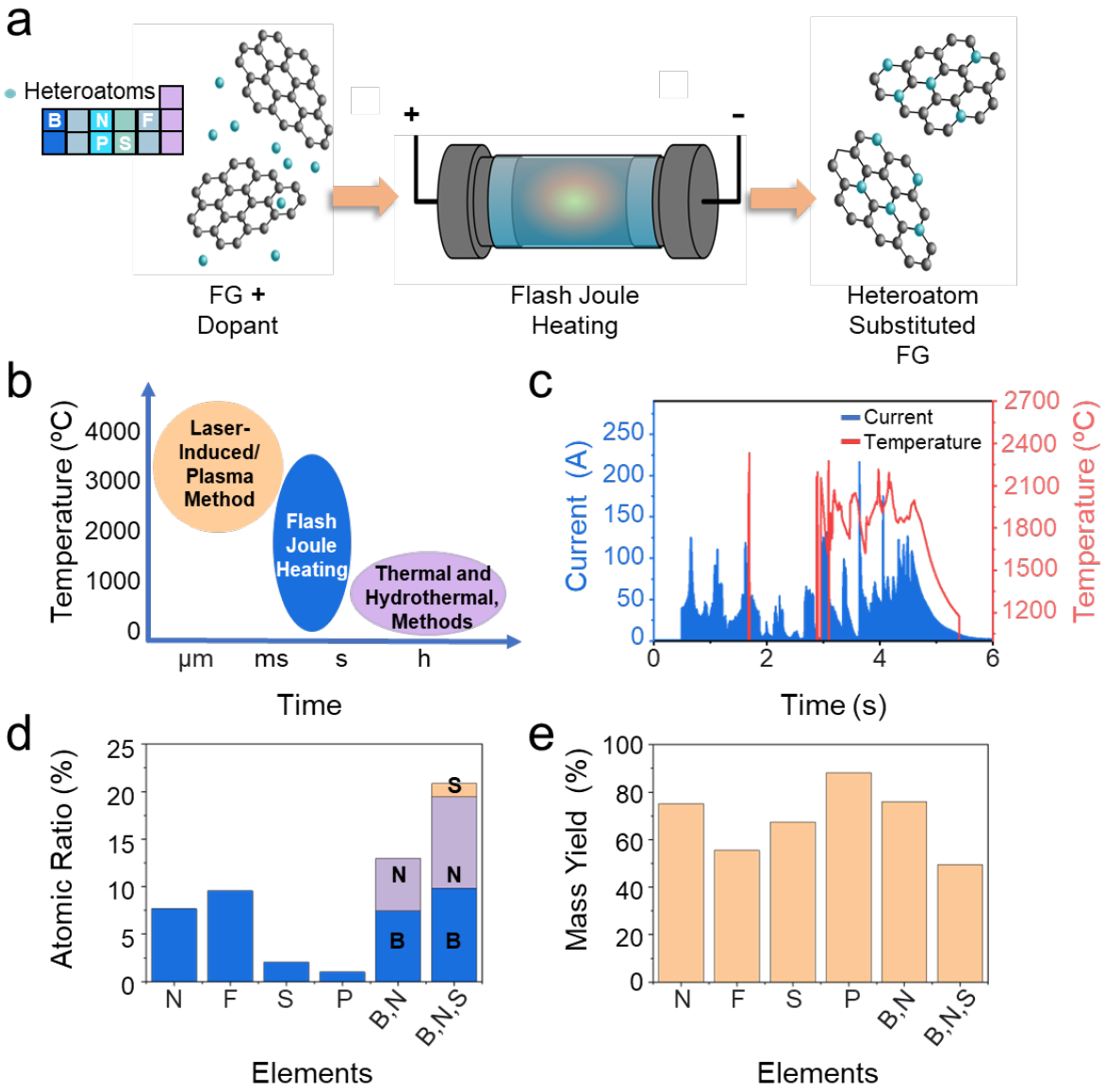

Figure 1. Synthesis of heteroatom-substituted-rFG from rFG. **a)** Schematic illustration of the heteroatom-substituted re-flash process. **b)** Temperature-time scale of the FJH process and other post treatment processes. **c)** Current and temperature profiles for P-rBACFG synthesis at 100 V. **d)** Atomic percentages of various heteroatoms substituted into BACFG. **e)** Reaction mass yield of different heteroatom substituted rBACFG.

2.2 Characterization of N-rBACFG

The analysis of N-rBACFG is illustrated in (Figure 2). Raman spectroscopy analysis was used to analyze the X-rFG quality, and additional details of the analyses are in the Methods section. In the Raman spectrum of N-rBACFG, three prominent peaks can be observed, including the 2D peak at ~2672 cm^{-1}, which arises from the second-order zone boundary phonons in graphene and is positively correlated with graphene crystallinity; the G peak at ~1570 cm^{-1}, which arises from the bond stretching of all pairs of sp^2 carbon atoms in the graphene rings; and the D peak at ~1339 cm^{-1}, which arises from the breathing mode of sp^2 carbon atoms in the graphene rings and is correlated with graphene defect density.[21,26,27] The ratio of the relative intensity of these peaks (known as the $I_{D/G}$) when comparing the D and G peaks, is proportional to the defect density and inversely proportional to sheet size.[8,26] The $I_{2D/G}$ ratio obtained when comparing the intensity of 2D and G peaks is correlated with graphene quality.[27] The graphene yield of a FG product is calculated by first selecting the Raman spectra with a discernible G peak and then counting the percentage that have a $I_{2D/G}$ ratio of at least 0.3.[28] An average spectrum comprised of 200 individual measurements of N-rBACFG (Figure 2a) shows a graphene yield of 99%, while the $I_{2D/G}$ was 0.69, and the $I_{D/G}$ ratio was 0.49. N-rBACFG exhibits higher Raman $I_{D/G}$ ratio compared to BACFG (Table S2) and thus a higher defect density, which is a positive indicator of heteroatom

doping.[8,11,29] In contrast, rFG without the presence of a heteroatom compound exhibits a lower $I_{D/G}$ ratio and thus lower defect density compared to single-flashed FG.[25] High resolution Raman measurement has confirmed that the rFG remains turbostratic based on the presence of the TS_1 peak at ~1873 cm^{-1} and TS_2 peak at ~2018 cm^{-1}, and the absence of a distinct M peak ~1750 cm^{-1}. An M peak would indicate ordered stacking (Figure 2b).[18,25]

BACFG has a strong (002) X-ray diffraction peak at 26.01˚, corresponding to an interlayer spacing of 3.431 Å (Figure S6), and is typical of turbostratic FG.[18] When BACFG is re-flashed at 80 V, the (002) peak shifts to a higher Bragg angle of 26.13˚, indicating a decrease in the graphene interlayer spacing to 3.412 Å (Figure S6) as the lattice becomes more ordered. In the presence of heteroatom sources such as melamine resin, nitrogen atoms appear incorporated into the graphene lattice through FJH. It is observed that the (002) peak of N-rBACFG (re-flashed at 80V) is 25.99˚, corresponding to an increase of the interlayer spacing to 3.432 Å (Figure 2c). This increase in interlayer spacing compared to unsubstituted rBACFG serves as a positive indication of heteroatom substitution. Throughout this discussion, X-rFG is compared to rBACFG, since both materials undergo the same two-step FJH process. This comparison allows for a more accurate evaluation of how heteroatom substitution affects the properties of BACFG, with observed differences more reliably attributed to the substitution process rather than variations in processing techniques.

To understand the relationship between interlayer spacing and the re-flash process, it is important to consider how variations in sample compression and conductivity prior to flash onset influence the discharge dynamics and subsequent structural changes in the graphene lattice. The flash duration is affected by the sample compression between the electrodes in that additional compression lowers the sample resistance, decreasing the capacitor discharge time constant.

Additionally, when phase changes such as melting or evaporation occur during the reaction, they can cause brief interruptions in the discharge as the electrical contact is momentarily broken and then reestablished within a few milliseconds.[18,22] Under the same compressive state BACFG is more conductive (lower resistance) than BACFG plus the melamine resin. Thus, the latter sample would experience longer discharge times. Since both samples are flashed with the same energy density, the sample that experiences the shorter discharge times will be subjected to higher temperatures, thus pushing the layers closer together. Overall, the re-flash process has two competing mechanisms that influence the interlayer spacing between the graphene sheets. First, the energy from the second flash pushes the layers together and second, heteroatom substitution increases the interlayer spacing. In the case of N-rBACFG the latter mechanism appears to be dominant, since the interlayer spacing increased overall.

More conclusively, X-ray photoelectron spectroscopy (XPS) is used to determine the atomic concentration of nitrogen in the graphene lattice as well as its distinct chemical states (Figure 2d). XPS analysis reveals that the total elemental ratio of nitrogen in the N-rBACFG sample is 7.68 at%. This level of nitrogen substitution is indicative of successful incorporation of nitrogen into the graphene structure, which is crucial for enhancing the material's properties. The deconvolution of the XPS N1s peak provides further insights into the chemical states of nitrogen within the particles. 68.84% of the N1s peak is due to pyridinic nitrogen (~398.7 eV), and 28% of the nitrogen is in the pyrrolic form (~399.8 eV). Pyridinic nitrogen is characterized by its six-member ring structure, and pyrrolic nitrogen is characterized by its five-membered ring structure. These two chemical states are typically found at the edges of the graphene lattice, at defect sites, or around pores[30,31] and can influence the material chemical reactivity.[32–34] A smaller fraction, 6.45%, is present as graphitic nitrogen. There was no indication of N-oxides in the XPS spectra.

The absence of N-oxides suggests that the nitrogen doping process did not introduce unwanted oxidation, which could compromise the material performance. To assess the reliability of the FJH method for nitrogen doping, we examined the nitrogen content from three different batches of N-rBACFG particles. The results are as follows: 7.68, 7.32, and 7.51 at%. The consistency of the nitrogen-substituted content across different batches highlights the reliability and reproducibility of the re-flashing method for producing uniformly doped materials.

XPS can also be used for depth analysis. A XPS depth scan was performed that consisted of etching the graphene particle to a calculated depth, in this case 20 nm using an argon ion gun, with subsequent analysis of the C1s and N1s peaks at each depth interval. As the N-rFG sample was etched, the C1s ratio decreased, indicating a reduction in the carbon content just below the surface. Concurrently, the N1s ratio increased, suggesting an enrichment of nitrogen atoms just below the surface layer. After the initial changes, both the C1s and N1s ratios plateaued, indicating a relatively stable composition at greater depths. A comprehensive depth profile analysis was conducted up to a depth of 140 nm, as shown in Figure 2e. The average concentration of N1s after etching to a depth of 140 nm was determined to be 6.81 at% with a standard deviation of 0.61%. This analysis revealed that the nitrogen substitution percentage remained relatively consistent throughout this depth change.

Brunauer–Emmett–Teller (BET) analysis was used to determine the surface area of BAC, BACFG, and N-rBACFG and is shown in Figure 2f. The respective values are 965, 115, and 30 m^2/g and are tabulated in Table S3. The reduction in surface area observed in the materials is primarily due to the re-flashing process and heteroatom substitution (Figure S7). The re-flashing process involves exposing the material to high temperatures over a short duration, which can lead to structural changes at the microscopic level. During this process, some of the micropores and

mesopores in the carbon structure can collapse or fuse, resulting in a reduction of the overall pore volume.[19] Additionally, substituting carbon atoms with heteroatoms such as nitrogen contributes to the reduction in surface area. The introduction of heteroatoms into the carbon lattice can cause alterations in the pore structure, including blocking or partially filling existing pores, thereby decreasing the accessible surface area.

Thermogravimetric analysis (TGA) of BACFG and N-rBACFG (Figure 2g) shows that both materials exhibit similar decomposition profiles when analyzed in air. The TGA curve for N-rBACFG indicates that no precursor material remains in the FJH product, suggesting that any nitrogen atoms present are incorporated into the graphene lattice. The TGA data also shows a difference in the temperature at which the major decomposition step occurs. For N-rBACFG, this major decomposition step takes place at 505 °C, whereas for the parent feedstock, it occurs at 593 °C. This major decomposition step typically represents the breakdown of the primary constituent of the material. The shift in the decomposition temperature is attributed to the substitution of some C-C bonds in BACFG with C-N bonds in the pyridinic and pyrrolic configurations. These seem to be the dominant constituents based on the XPS analysis. The C-N bonds are easier to oxidize compared to C-C bonds, leading to the lower decomposition temperature observed for N-rBACFG. This substitution and the resulting thermal behavior confirm the successful substitution of nitrogen into the graphene lattice. Thus, as expected, BACFG is more oxidatively stable than N-rBACFG. The corresponding heat flow curves are shown in Figure S8.

Transmission electron microscopy (TEM) images of the graphene products (Figure 2h-i) reveal nm-sized graphene sheets with visible crystalline lattice fringes, indicative of high crystalline quality. The fast Fourier transform (FFT) inset shows a diffraction pattern and turbostratic stacking of the graphitic domains, confirming well-defined crystalline structures.

Further TEM analysis in Figure S9 corroborated these findings. The average interlayer spacing determined by TEM was 0.343 nm (Figure S9), which is consistent with the value determined by XRD. Bright field scanning transmission electron microscopy (BF-STEM), high-angle annular dark field scanning transmission electron microscopy (HAADF-STEM) images and energy dispersive X-ray spectroscopy (EDS) elemental mapping in Figures S10-11 demonstrate the uniform distribution of nitrogen within the N-rBACFG, validating the substitution process and structural integrity of the material.

We further demonstrated that this post-treatment synthesis technique can be scaled up. 3 g of N-rBACFG were produced using a pretreatment flash of 150 V and a main flash of 300 V. This scaled reaction was performed in a 16 mm inner diameter, 7 cm long fused quartz tube and was placed into a larger sample holder connected externally to the FJH system. As indicated in Figure S12, atomic substitution reached levels of up to 5.69 at% of N. The scalability of this method further provides a pathway for large-scale production of heteroatom-substituted carbon materials. The versatility of this technique was demonstrated through nitrogen substitution and functionalization of other feedstocks, such as MCFG. As illustrated in Figure S13, the XPS analysis of N-rMCFG showed an atomic nitrogen ratio of 8.62 at%. This suggests that various carbon feedstocks can be effectively used for heteroatom substitution, expanding the applicability of this method. The ability to adapt the process to different carbon sources without losing efficiency in nitrogen substitution enhances the potential for generating advanced materials with optimized performance characteristics.

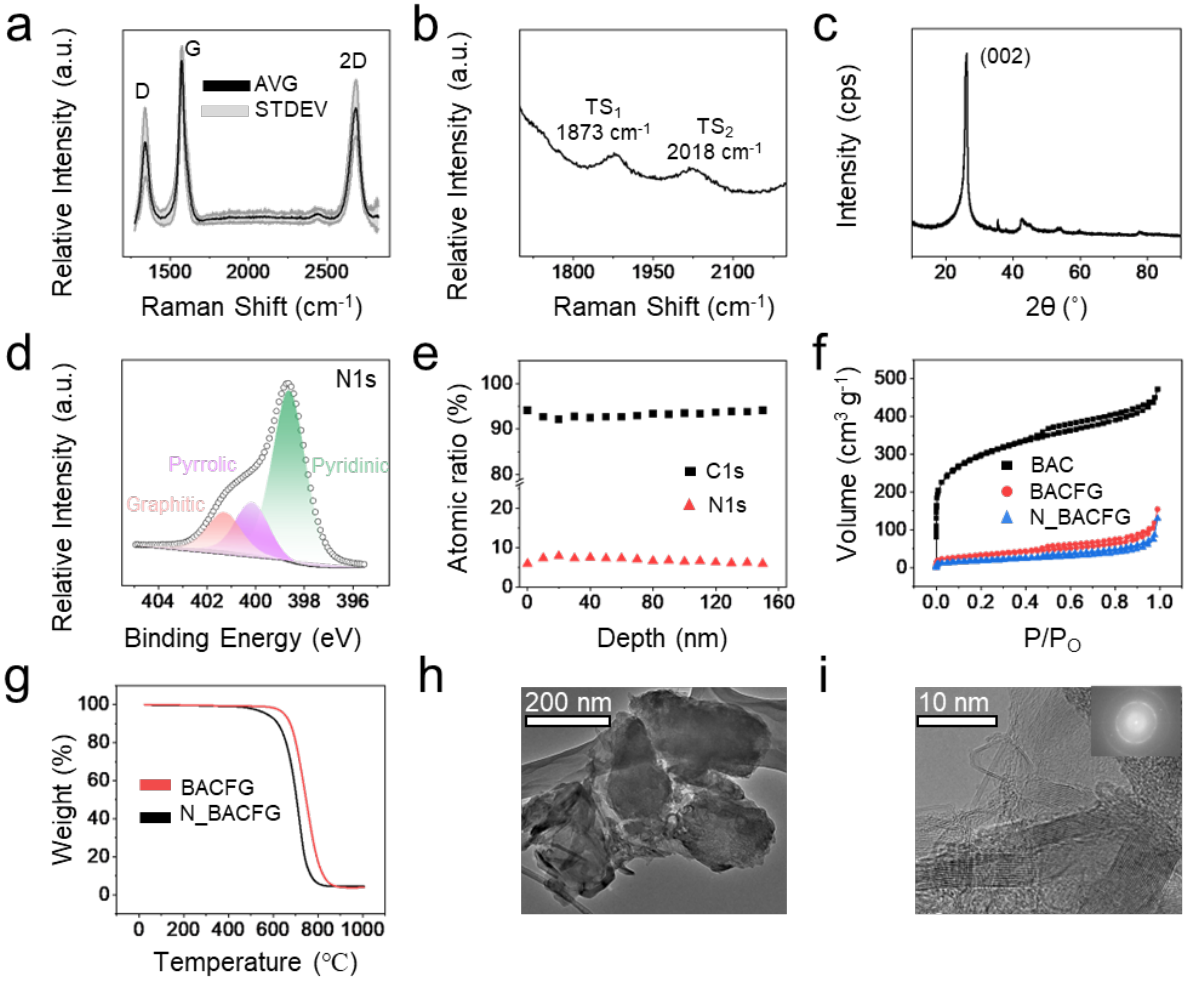

Figure. 2 Spectroscopic spectra and microscopic images of N-rBACFG. **a)** Average Raman spectra of N-rBACFG. **b)** High resolution Raman spectrum showing the presence of TS_1 and TS_2 peaks and the absence of the M peak confirms the turbostratic stacking of the graphene in these samples.[1,4] **c)** XRD pattern of N-rBACFG. The intensity of the pattern is expressed in counts per second (cps). **d)** Deconvolution of the XPS N1s peak. The total nitrogen concentration is 7.68%. **e)** XPS depth scan analysis of N-rBACFG. **f)** BET surface area analysis **g)** TGA comparison of N-rBACFG and the starting material BACFG in air from 25 to 1000 ºC at a ramp rate of 10 ºC/min. **h)** TEM image of N-rBACFG. **i)** Higher magnification TEM image from the same region of Figure 2h. The inset shows an FFT.

2.3 Characterization of other Types of Heteroatoms Substituted BACFG and Scaling-Up

FJH was previously demonstrated to synthesize a range of heteroatom-doped FG, thus demonstrating the universality of this technique.[8] Here we show that utilizing FJH as a post treatment synthesis technique can yield a range of heteroatom-substituted FG. Heteroatoms have differing atomic radii and electronegativity compared to carbon. Hence, when heteroatoms are incorporated into the graphene lattice, lattice mismatch occurs as well as re-distribution of electrons within the bond. Nitrogen is 5.3% smaller than carbon, with atomic radii of 71 pm and 75 pm, respectively. In contrast, sulfur is 38.7% larger than carbon, with an atomic radius of 104 pm. The lattice mismatch would be much greater if sulfur is incorporated into the graphene lattice and could even interrupt lattice stacking. Large atoms such as phosphorus might protrude from the graphene plane due to the C-P bond being ~25% longer than the C-C bond.[35] Thus, the incorporation of larger atoms into graphene tends to occur at a much lower atomic ratio compared to atoms with radii comparable to that of carbon.[11] As a result, we expect that atoms with smaller radii (N or B) can be incorporated into the lattice at higher atomic ratios. Monovalent elements such as fluorine typically bind to the edge of the graphene sheet. The bond may be covalent and or semi-ionic. The introduction of these heteroatoms can increase the D peak in the Raman spectra (Figures 3a, d, g) due to a lowering of the lattice symmetry. The interlayer spacing due to these heteroatoms can also increase up to ~6.5 % in some cases (Figures 3b, e, h). Here the atomic ratios of F, S, and P-substituted rFG are 9.55, 2.06, and 1.01 at%, respectively (Figures 3c, f, i). Additional TEM and HAADF STEM and EDS characterization is shown in Figures S14-16.

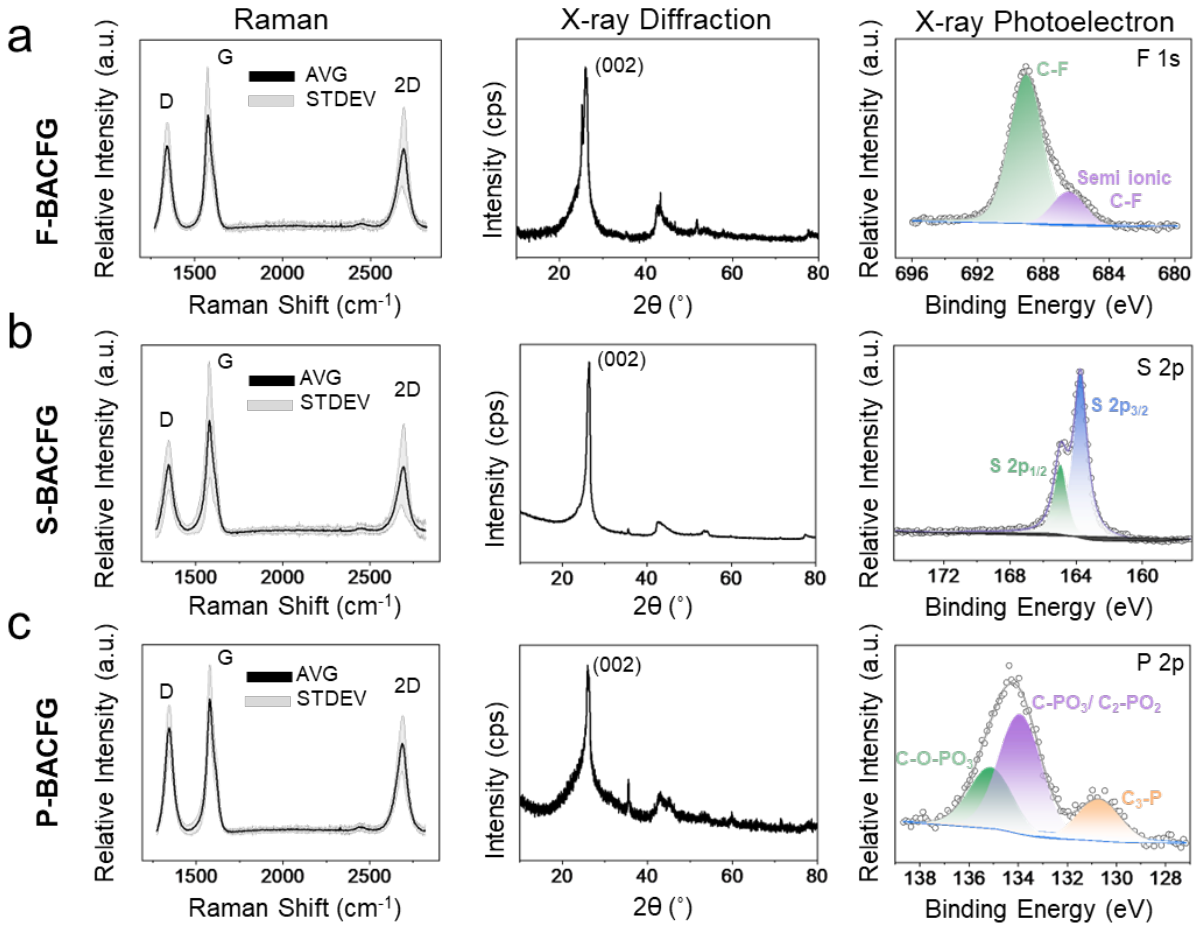

Figure 3. Characterization of heteroatom-substituted flash graphene. Raman, XRD, and XPS spectra for **a-c)** F-rBACFG, **d-f)** S-rBACFG and **g-i)** P-rBACFG. Each Raman measurement was performed across 100 points, each measured twice. The average Raman spectrum is illustrated as the black line, and the standard deviation is illustrated as the gray region around the average spectrum.

Heteroatoms from multiple different elements can also be substituted into the graphene lattice simultaneously. This is referred to as co- or multi-elemental substitution. Boron-nitrogen and boron-nitrogen-sulfur combinations form B,N-rBACFG and B,N,S-rBACFG, respectively. The elements collectively incorporate into the graphene lattice at higher at% than by single atom

substitution. The precise control of the substitution process and the selection of appropriate heteroatom feedstocks are crucial for optimizing the performance of co-substituted graphene in various applications. After co- and triple-heteroatom substitution, the graphene remains crystalline, as shown by the Raman and the XRD spectra (Figure 4a-b and 4f-g). However, the graphene yield and crystallinity decreased, as seen by the decrease in the height of the 2D peak, (Table S2) likely due to the high at% of heteroatoms substituted into the graphene lattice. The total at% of heteroatoms were 12.95 and 20.87 at% for B,N-rBACFG and B,N,S-rBACFG, respectively. This represents a 25% to 55% increase in total heteroatom content compared to previously reported values.[8] XPS high resolution elemental mapping shows the chemical state deconvolution of the various heteroatoms in Figure 4c-d and 4h-j. The N1s peak exhibits a similar ratio across the different chemical states, whereas the B1s peak reveals that B,N-rBACFG has a higher proportion of the graphitic boron state, while B,N,S-rBACFG shows a predominance of the borinic chemical state. TEM was used to observe the morphology of the resultant product Figure 4e, k. HAADF STEM and EDS characterization of B,N-rBACFG and B,N,S -rBACFG are shown in Figures S17-18, respectively.

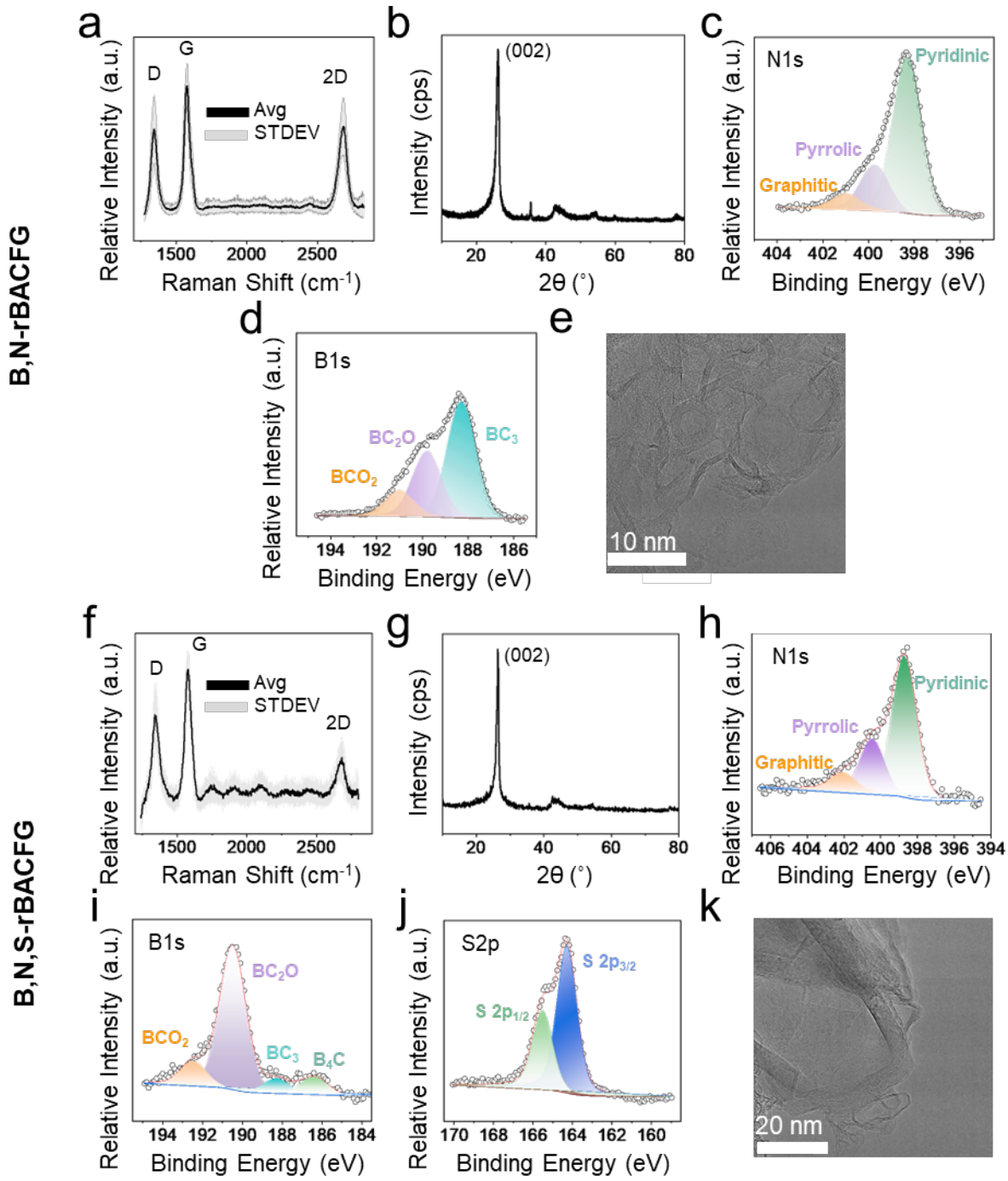

Figure 4. Characterization of heteroatom multi-substituted rBACFG. **a-e)** Characterization of B,N-rBACFG. **f-k)** Characterization of B,N,S-rBACFG **a)** Average Raman spectrum; the black line and the gray shadow represent the average value and the standard deviation of 200 measurements across 100 sampling points, respectively. **b)** XRD pattern. **c-d)** XPS elemental

analysis. **e)** TEM image of the graphitic sheets. **f)** Raman spectra for B,N,S-rBACFG. **g)** XRD pattern. **h-j)** XPS elemental analysis. **k)** TEM image.

2.4 Applications of N-rBACFG

The rBACFG and N-rBACFG are further evaluated as the anode material for lithium-ion batteries (LIBs). The rBACFG and N-rBACFG anodes exhibit a superior capacity of over 300 mAh g^{-1} at 0.2 C. However, the capacity of rBACFG decreased to ~34% of its initial value at 500^{th} cycles. Benefitting from uniform nitrogen substitution on the graphene surface, N-rBACFG exhibited higher capacity retention (~93% at 500 cycles) and better rate performance. The enhanced battery performance suggests that the FJH process is important in converting low-cost carbon feedstock into valuable graphene-based anode material and modulating its properties by efficient heteroatom substitution.

The rBACFG shows turbostratic structure, which is verified by the XRD, Raman and high-resolution TEM images as previously discussed. The expanded layer spacing in turbostratic graphene allows the fast intercalation kinetics of lithium-ion and makes rBACFG suitable to be used as the anode materials in LIBs.

We applied the rBACFG and N-rBACFG as the anode in a coin cell with lithium chips serving as the counter electrode. The battery performances of rBACFG and N-rBACFG anodes were further compared. After the initial activation cycles at 0.05 C, the stability of the batteries was evaluated at 0.2 C. Comparable initial capacity (~310 mAh/g) was observed in rBACFG and N-rBACFG anodes (Figure 5a). However, the long-term galvanostatic discharge-charge cycling results (Figure 5a-c) indicate a higher capacity retention of 93% after 500 cycles in N-rBACFG compared to a capacity retention of 34% after 500 cycles in BACFG. The average specific capacity

of the N-rBACFG anode is 316, 267, 239, 194 and 114 mAh·g^{-1} at the rate of 0.1 C, 0.2 C, 0.5 C, 1 C and 2 C, respectively, all of which exhibit enhanced performances compared to those of the BACFG counterpart (Figure 5d).

After cycling, cracks and some particles can be detected on the solid electrolyte interphase (SEI) layer in the rBACFG anode (Figure S19). A more uniform and continuous SEI layer formed on the N-rBACFG anode (Figure S19). HR-TEM images (Figure S20) showed an extended crystallized region on N-rBACFG particles after cycling. Well-crystallized turbostratic graphene layers were identified on the N-rBACFG surface before cycling (Figure S20). The 0.343 nm lattice spacing corresponds to (002) plane of the turbostratic graphene. The anode was disassembled from the battery and characterized for comparison after 200 cycles. The thickness of the crystalline region increased from ~10 nm to ~30 nm after cycling. These results suggest that nitrogen atoms are critical to interact with the Li^+ intercalation and form the continuous crystalline carbon structure.

We further investigated the mechanism of improved LIB performance of N-rBACFG by electrochemical measurements. First, cyclic voltammetry (CV) was performed to assess the Li^+ diffusion kinetics (Figures 5e, 5f). For both rBACFG and N-rBACFG anodes, with increasing potential scan rate, all CV curves exhibit similar shapes during the lithiation/delithiation processes, suggesting the reversible Li^+ insertion and extraction, and low polarization. Generally, Li^+ storage includes two parts: the diffusion-controlled Faradaic reaction process and the surface-induced capacitive process. The contribution of these two processes can be evaluated with Equation 2:

$$i = av^b \qquad (2)$$

where i is the current, v is the scan rate, a and b are scaling constants.[36] The b value, calculated from the slope of log(i) plotted as a function of log(v), which is ~0.5, indicates that the

Li^+ diffusion process is the dominant process for both rBACFG and N-rBACFG anodes (Figure 5g).

To investigate the Li^+ diffusion behavior in both anodes, the diffusion coefficients were quantitatively measured by the galvanostatic intermittent titration technique (GITT).[37] The detailed experimental and calculation processes of Li^+ diffusion coefficients are shown in Supporting Section 3 and Figure S21. N-rBACFG shows a higher Li^+ diffusion coefficient than the rBACFG, especially at the range of 0.4 - 0.8 V. The results suggest a faster Li^+ diffusion kinetics in the nitrogen-substituted graphene shell. It is possibly related to the increased crystalline carbon region formation after the initial Li^+ intercalation. Finally, the charge-transfer resistances before cycling and after 200 cycles were compared in Figure 5i. Electrochemical impedance spectroscopy spectra reveal a lower charge-transfer resistances of N-rBACFG (R_{ct} = 48 Ω, corresponding to the semicircle in the high-to-medium frequencies) compared with that of the BACFG anode (R_{ct} = 63 Ω, Figure 5g). After 200 cycles, the R_{ct} maintained a similar value in N-rBACFG, while it increased by 50% in rBACFG. The result suggests a higher-charge transfer rate of N-rBACFG anode and the resistance buildup in the rBACFG anodes likely due to undesired side reactions on the surface. The slope in the low-frequency region is related to the Li^+ diffusion process. The higher slope of N-rBACFG anode suggests its higher Li^+ diffusion efficiency, which is consistent with the GITT results. Based on our results, it can be concluded that nitrogen-substitution in the rFG structure is important to construct a highly stable SEI layer in the rBACFG material, which is necessary to sustain the high-performance anode in LIBs.

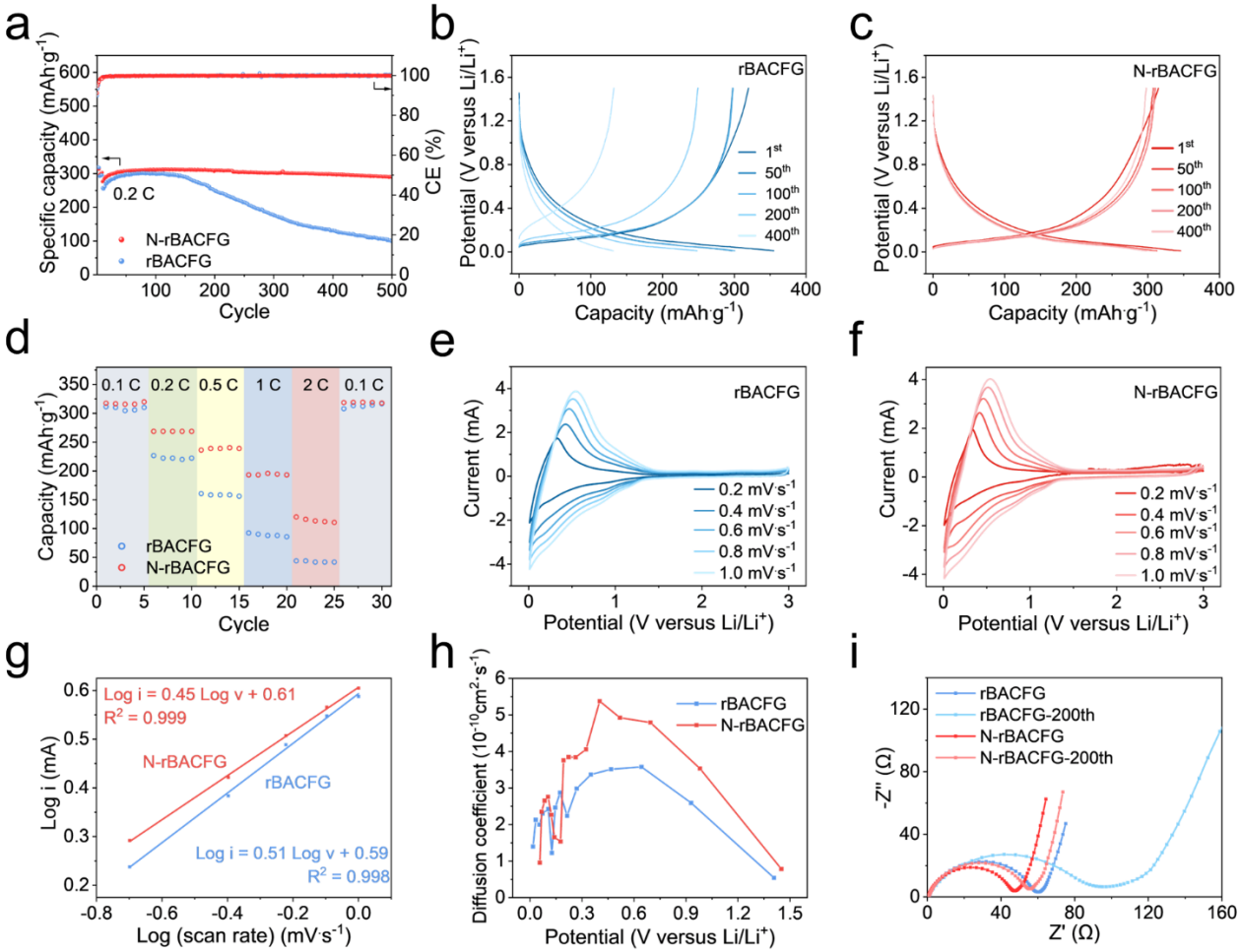

Figure 5. LIB performance of BACFG and N-BACFG anode. **a)** Cycling stability of rBACFG anode (blue spot) and N-rBACFG anode (red spot) at 0.2 C. **b)** Charge-discharge profiles of rBACFG anode at different cycles. **c)** Charge-discharge profiles of N-rBACFG anode at different cycles. **d)** Rate capacity of BACFG anode (blue spot) and N-rBACFG anode (red spot). **e)** CV curves of rBACFG anode at different scan rates. **f)** CV curves of N-rBACFG anode at different scan rates. **g)** The fitting lines of peak current density and potential scan rate in CV curves of rBACFG and N-rBACFG. **h)** The Li^+ diffusion coefficient of BACFG anode (blue line) and N-rBACFG anode (red line) during the charging process. **i)** Nyquist plots of rBACFG anode (blue lines) and N-rBACFG anode (red lines) before and after cycling.

To further understand the factors influencing the electrochemical performance of the anodes, we examined the concentration of various transition metals using inductively coupled plasma mass spectrometry (ICP-MS) (Figure S22). Metals such as Ni, Fe, Co, Mn, Zn and V came from the starting BAC material, and their concentration decreased after FJH. Other metals such as Cu, Ti and W increased in concentration after FJH and likely came from the electrodes. The metal concentration of the rBACFG and N-rBACFG was comparable; thus, it is unlikely that the trace metals contributed to the electrochemical differences between these materials.

N-rBACFG was also added to vinyl ester resin to form polymer composites, and some mechanical properties are shown in Figures S23-S25. Nanoindentation studies of N-rBACFG in VE showed an increase on ~42 % and ~46 % in the Young's modulus and hardness, respectively, when 3 wt% of heteroatom-substituted filler was added, compared to the neat polymer composite. The thermal properties of N-rBACFG when added to epoxy resin to form a polymer composite were investigated Figure S26-27, with no significant changes observed.

To understand the environmental and economic impact of a material or process, a life cycle assessment (LCA) and technoeconomic analysis (TEA) are commonly employed.[38] LCA systematically evaluates the environmental impact of a product, process, or service throughout its life span or up to specific points in its life cycle. For instance, a cradle-to-gate LCA considers stages from raw material extraction through manufacturing, distribution, and use, excluding disposal or recycling. Complementary to this is a TEA, which assesses cost inputs and outputs based on LCA data. Together, LCA and TEA provide a comprehensive estimate of environmental and economic burdens, enabling more informed decisions to reduce negative impacts. These models are widely used in sustainability practices to identify improvement opportunities and support eco-friendly product design and resource management.[39–41] The GREET software

provided data for analyzing energy consumption and greenhouse gas emissions for the reactants and processes involved. However, since the GREET database lacked information on most of the heteroatom sources used in this study, this LCA focuses on PVDF as the heteroatom source for producing F-rFG, as data for this material was available. This approach allowed for a more accurate and relevant analysis of the environmental and economic impacts of heteroatom substitutions via the re-flashing method.

The energy use, water use, and CO_2 equivalent emissions of the various production steps and processes are shown in Figure S28**.** The production of the raw material, BAC had the highest energy contribution, water use and CO_2 emissions at 210 MJ/kg, 3.8 L/kg and 11 kg/kg respectively. F-rBACFG can thus be produced by this method at only $5.73/kg. The values used in this LCA were determined by the GREET software and from our experimental data.

Conclusions

Various types of heteroatom-substituted rFG were synthesized by this scaled-up, post treatment method. This includes single element substitution of N-rFG, F-rFG, P-rFG S-rFG, B,N-rFG co-substituted, and B,N,S-rFG triple co-substituted. As with our previous *in situ* method, these reactions are solvent free, water free, catalyst free, in the solid state, and occur on the timescale of a few seconds. Since the reactions occurred in an unsealed reaction chamber, the boiling point of the dopant was considered. Melamine resin has a higher boiling point than melamine, so the former was chosen as the primary nitrogen dopant to minimize volatilization and off-gassing. Overall, several low-cost heteroatoms sources were used to form high quality heteroatom-substituted rFG.

The re-flash process has two competing mechanisms; the second flash was shown to push the layers of the turbostratic graphene closer together, while doping slightly increases the interlayer

separation depending on the atom. N-rBACFG as a representative material was used as the anode in Li ions batteries and demonstrated improved stability over 500 cycles compared to rBACFG (without any heteroatoms), owing to a highly stable SEI layer, which is necessary to maintain long term stability and performance. The heteroatom substituted graphene can also be used as a filler for polymer composites. A LCA of F-rFG assessed the energy consumption, water use and greenhouse gas emissions of the materials and processes and revealed that the production of BAC, the main carbon feedstock, was the major contributor to impacts in each category. Meanwhile, the TEA revealed that F-rFG can be produced for only $5.73 per kg, highlighting its economic viability for large-scale applications.

Experimental Section

Materials

Bituminous activated charcoal (BAC) was obtained from Charcoal House (SKU C-347) at 4x12 mesh. Nitrogen doping was achieved using melamine formaldehyde resin obtained from U.S. Chemical (MF 415). Boric acid (31768-453.6G, 99.9%) was purchased from Baker Analyzed Reagent. Poly(1,4-phenylene sulfide) (PPS, 182354-100G, average MW∼10,000) and perfluoro octane sulfonic acid was purchased from Millipore-Sigma. Red phosphorus (343242-5G, 99.99%) was purchased from Millipore-Sigma. *N*-Methyl-2-pyrrolidinone (NMP, 99.5 wt%) was purchased from Millipore-Sigma. The polyvinylidene fluoride binder (PVDF) and lithium chips (16 mm diameter, 0.6 mm thickness, 99.9 wt%) were purchased from MTI Corporation. Acetylene black (ABHC-01) was purchased from Soltex Corporation. 1 M $LiPF_6$ (battery grade) was purchased from Millipore-Sigma. Ethylene carbonate (EC), diethyl carbonate (DEC) and dimethyl carbonate (DMC) were purchased from Millipore-Sigma.

Characterization

Raman spectra were collected using a Renishaw Raman microscope equipped with a 532 nm 5 mW laser and LiveTrack software to automatically adjust the focus between measurements. Custom Python scripts were used to analyze the Raman spectra and identify the presence and the peak intensity of the D, G, and 2D peaks present in graphene, using a previously reported analysis procedure.[28] For each sample, 2 measurements were performed on each of 100 points across a square 1 mm^2 grid. The average of these 200 measurements comprises each spectrum illustrated in this paper. To calculate the $I_{2D/G}$ and $I_{D/G}$ peak ratios, custom Python scripts first select from among these 200 measurements the spectra with discernible G peaks. Failure to identify a G peak indicates that the Raman measurement was unfocused, so that data point is discarded. Among this subset of ~190 measurements, the average $I_{2D/G}$ and $I_{D/G}$ peak ratios are calculated. The number of measurements recording an $I_{2D/G}$ ratio of ≥ 0.3 is then divided by the total number of spectra with a discernible G peak. This result is the graphene yield.

X-ray diffractometry (XRD) scans were performed using a Rigaku Smartlab II using zero background sample holders, a 40 kV, 30 mA X-Ray source, and a Cu K-β filter. Scanning electron microscopy (SEM) images were collected at high vacuum with an FEI Quanta 400 ESEM FEG equipped with SE, backscatter, and EDS detectors. The surface chemical composition was determined by X-ray photoelectron spectroscopy (XPS, Shimazu-Kratos AXIS UTLTRA DLD) using a monochromated Al Kα source. Survey spectra were recorded using 0.5 eV step sizes with a pass energy of 140 eV. Elemental spectra were recorded using 0.1 eV step sizes with a pass energy of 26 eV. All the XPS spectra were corrected using the C 1s peaks (284.8 eV) as reference.

The surface area and pore structure were characterized on an automated gas sorption analyzer (Autosorb-iQ, Quantachrome) with N_2 as adsorbate. The specific surface areas of the

samples were determined from the nitrogen adsorption/desorption isotherms by using the Brunauer–Emmett–Teller (BET) method, whereas the pore size distribution curves were derived from the Barrett–Joyner–Halenda (BJH) method (for mesopores) and the density functional theory (DFT) approach (for micropores).

Transmission electron microscopy (TEM) images were collected using FEI Titan Themis operating at 300 keV with a convergence angle of 25 m rad. The aliquot of sample (5 mg of sample/1 mL ethanol) was prepared and was sonicated for 1 h to ensure homogeneous dispersion. The resultant aliquot was drop casted on Cu/lacey carbon TEM grid (Ted Pella). The resultant grid was dried at 80 °C with overnight vacuum drying.

The filtrates of the washed samples post-FJH were diluted using 2% HNO_3 and analyzed using ICP-MS. For the extraction, 50 mg of BAC, rBACFG and N-rBACFG were digested using 20 mL of 2% HNO_3 at room temperature for 24 h. The filtrate was further diluted and analyzed. The Cr, Ni, Zn, Mn, V, W, Mo , Mg, Cu, Fe, Co, Ti, Pt, Au, Ir, Ru, and Pd were measured by inductively coupled plasma mass spectrometry (ICP-MS) using a Perkin Elmer Nexion 2000B ICP-MS system, with Periodic Table Mix 1 for ICP (10 mg L^{-1}, 10 wt% HNO_3, MilliporeSigma) as the standard. The standard solutions were prepared with 1, 5, 10, 25, 50, 100 ppb concentrations by diluting the original Mix 1 and 2 solutions with 2 wt% HNO_3 solution. The sample concentration was calculated from the calibration curve. The sample was diluted to the appropriate concentration using 2 wt% HNO_3 within the calibration curve range.

Flash Joule Heating

Flash Joule heating was conducted utilizing a previously reported 0.624 F capacitor-based system.[3] This system employs 1 kHz pulse width modulation of the discharge pulse with a duty cycle sequence of 10% for 1 s, 20% for 0.5 s, 50% for 5 s. After the 6.5 second flash, the final

voltage is generally < 10 V. For the re-flash heteroatom vessel, an 8 mm inner diameter quartz tube is used with a length of ~6 cm. The mixture is loaded into the center and is held between two cylindrical conductive graphite "spacers." The spacer is 8 mm in diameter and ~8 mm in length. 0.5 g of copper wool is added to each end to enhance the electrical contact. The sample in the quartz tube is then placed between two outer brass electrodes, which are connected to the flash Joule heating system. The scaled reaction was performed using a 16 mm inner diameter quartz tube with a length of 7 cm.

Electrochemical tests

The rBACFG and N-rBACFG powders, acetylene black and PVDF binder were milled and mixed to prepare the slurry with a mass ratio of 8:1:1. NMP was used as the solvent. The slurry was coated on an 8 μm-thick copper foils by the doctor blade and dried in a built-in heating cover at 70 °C for 2 h, followed by drying in a vacuum oven at 70 °C under vacuum (~10 mmHg) overnight. The average loading density of the active materials was ~4.0 mg with a diameter of 14 mm. The coin cells were assembled in an argon filled glove box with moisture and oxygen concentration below 1 ppm. Lithium chips were used as the counter electrode with an Al_2O_3 ceramic coated polypropylene separator (~26 μm, SH416W14, SENIOR INC.). 1 M $LiPF_6$ salt dissolved in a mixture of ethylene carbonate (EC), dimethyl carbonate (DMC) and diethyl carbonate (DEC) (1:1:1 vol%) was used as the electrolyte with 60 μL for each cell. Galvanostatic charge-discharge cycling of cells was conducted in the potential window from 0.01 to 1.5 V and all cells were cycled at 0.05 C for 5 cycles and 0.1 C for 5 cycles before cycling at 0.2 C for stability tests. Cyclic voltammetry (CV) voltammograms were taken with different scan rates in the range of 0.01–3.0 V using a CHI 680D electrochemical workstation. Electrochemical impedance spectroscopy measurements were conducted on the CHI 680D electrochemical

workstation by applying an alternating voltage of 5 mV over the frequency ranging from 0.01 Hz to 1 MHz. SEM images of cycled batteries were acquired by disassembling batteries after 200 cycles in the argon-filled glovebox. The SEM stages were sealed under argon and transferred to SEM chamber quickly to avoid oxidation.

Nanoindentation was carried out using a Hysitron TI 980 Triboindenter equipped with a Berkovich tip with a pyramidal geometry. To calculate the indentation modulus and hardness, at least five different indentations were performed for each sample with a maximum displacement of 100 nm and a displacement rate of 10 nm s^{-1}.[42]

Stress–strain curves were obtained through uniaxial compressive tests at room temperature with a standard compressive testing machine (MTS Model 312.21). Samples of varying thickness (11 to 15 mm) and diameter (~25 mm) were held between two crossheads, checked to avoid misalignment, and then compressed at a constant rate of 2 mm min^{-1}. Strain was calculated based on the individual thickness of each sample, given the varying thicknesses.[42]

Acknowledgements

The funding of the research was provided by the Air Force Office of Scientific Research (FA9550-22-1-0526, J.M.T.), the U.S. Army Corps of Engineers, ERDC (W912HZ-21-2-0050 and W912HZ-24-2-0027, J.M.T.) and the Welch Foundation (C-2065-20210327, Y.H.). L.C and G.W acknowledge the Building Technologies Office (BTO) IBUILD- Graduate Research Fellowship administered by the Oak Ridge Institute for Science and Education (ORISE) and managed by Oak Ridge National Laboratory (ORNL) for the U.S. Department of Energy (DOE). ORISE is managed by Oak Ridge Associated Universities (ORAU), and ORNL is managed by UT-Battelle LLC. All opinions expressed in this paper are the authors' and do not necessarily reflect the policies and

views of DOE, EERE, BTO, ORISE, ORAU, ORNL or UT-Battelle. ORISE is managed by ORAU under DOE contract number DE-SC0014664, and ORNL is managed by UT-Battelle LLC under DOE contract number DE-AC05-00OR22725. C.-H.C. and Y.H. acknowledges the Welch Foundation (C-2065), and the American Chemical Society Petroleum Research Fund (67236-DNI10). The characterization equipment used in this project is partly from the Shared Equipment Authority (SEA) at Rice University.

References

1. Geim, A. K.; Novoselov, K. S. The Rise of Graphene. *Nat. Mater.* **2007**, *6*, 183–191.
2. Papageorgiou, D. G.; Kinloch, I. A.; Young, R. J. Mechanical Properties of Graphene and Graphene-Based Nanocomposites. *Prog. Mater. Sci.* **2017**, *90*, 75–127.
3. Castro Neto, A. H.; Guinea, F.; Peres, N. M. R.; Novoselov, K. S.; Geim, A. K. The Electronic Properties of Graphene. *Rev. Mod. Phys.* **2009**, *81*,109–162.
4. Balandin, A. A. Thermal Properties of Graphene and Nanostructured Carbon Materials. *Nat. Mater.* **2011,** *10*, 569–581.
5. Deka, M. J.; Chowdhury, D. Tuning Electrical Properties of Graphene with Different π-Stacking Organic Molecules. *J. Phys. Chem. C* **2016**, *120*, 4121–4129.
6. Zhou, J.; Wu, M. M.; Zhou, X.; Sun, Q. Tuning Electronic and Magnetic Properties of Graphene by Surface Modification. *Appl. Phys. Lett.* **2009**, *95*, 103108.
7. Burgess, J. S.; Matis, B. R.; Robinson, J. T.; Bulat, F. A.; Keith Perkins, F.; Houston, B. H.; Baldwin, J. W. Tuning the Electronic Properties of Graphene by Hydrogenation in a Plasma Enhanced Chemical Vapor Deposition Reactor. *Carbon* **2011**, *49*, 4420–4426.

8. Chen, W.; Ge, C.; Li, J. T.; Beckham, J. L.; Yuan, Z.; Wyss, K. M.; Advincula, P. A.; Eddy, L.; Kittrell, C.; Chen, J.; Luong, D. X.; Carter, R. A.; Tour, J. M. Heteroatom-Doped Flash Graphene. *ACS Nano* **2022**, *16*, 6646–6656.

9. Zhang, C.; Fu, L.; Liu, N.; Liu, M.; Wang, Y.; Liu, Z.; Zhang, C. H.; Fu, L.; Liu, N.; Liu, Z. F.; Liu, M. H.; Wang, Y. Y. Synthesis of Nitrogen-Doped Graphene Using Embedded Carbon and Nitrogen Sources. *Adv. Mater.* **2011**, *23*, 1020–1024.

10. Lv, R.; Terrones, M. Towards New Graphene Materials: Doped Graphene Sheets and Nanoribbons. *Mater. Lett.* **2012**, *78*, 209–218.

11. Wang, X.; Sun, G.; Routh, P.; Kim, D.-H.; Huang, W.; Chen, P. Heteroatom-Doped Graphene Materials: Syntheses, Properties and Applications. *Chem. Soc. Rev.* **2014**, *43*, 7067–7098.

12. Xu, H.; Ma, L.; Jin, Z. Nitrogen-Doped Graphene: Synthesis, Characterizations and Energy Applications. *J. Energy Chem.* **2018**, *27*, 146–160.

13. Bepete, G.; Voiry, D.; Chhowalla, M.; Chiguvare, Z.; Coville, N. J. Incorporation of Small BN Domains in Graphene During CVD Using Methane, Boric Acid and Nitrogen Gas. *Nanoscale* **2013**, *5*, 6552.

14. Jung, S.; Lee, E. K.; Choi, M.; Shin, D.; Jeon, I.; Seo, J.; Jeong, H. Y.; Park, N.; Oh, J. H.; Baek, J. Direct Solvothermal Synthesis of B/N-doped Graphene. *Angew. Chem.* **2014**, *126*, 2430 –2433.

15. Jeon, I. Y.; Choi, H. J.; Ju, M. J.; Choi, I. T.; Lim, K.; Ko, J.; Kim, H. K.; Kim, J. C.; Lee, J. J.; Shin, D.; Jung, S. M.; Seo, J. M.; Kim, M. J.; Park, N.; Dai, L.; Baek, J. B. Direct Nitrogen Fixation at the Edges of Graphene Nanoplatelets as Efficient Electrocatalysts for Energy Conversion. *Sci. Rep.* **2013**, *3*, 1-7.

16. Jun, G. H.; Jin, S. H.; Lee, B.; Kim, B. H.; Chae, W.-S.; Hong, S. H.; Jeon, S. Enhanced Conduction and Charge-Selectivity by N-Doped Graphene Flakes in the Active Layer of Bulk-Heterojunction Organic Solar Cells. *Energy Environ. Sci.***2013**, *6*, 3000.

17. Jeong, H. M.; Lee, J. W.; Shin, W. H.; Choi, Y. J.; Shin, H. J.; Kang, J. K.; Choi, J. W. Nitrogen-Doped Graphene for High-Performance Ultracapacitors and the Importance of Nitrogen-Doped Sites at Basal Planes. *Nano Lett.* **2011**, *11*, 2472–2477.

18. Luong, D. X.; Bets, K. V; Algozeeb, W. A.; Stanford, M. G.; Kittrell, C.; Chen, W.; Salvatierra, R. V; Ren, M.; Mchugh, E. A.; Advincula, P. A.; Wang, Z.; Bhatt, M.; Guo, H.; Mancevski, V.; Shahsavari, R.; Yakobson, B. I.; Tour, J. M. Gram-Scale Bottom-up Flash Graphene Synthesis. *Nature* **2020**, *577*, 647–651.

19. Stanford, M. G.; Bets, K. V.; Luong, D. X.; Advincula, P. A.; Chen, W.; Li, J. T.; Wang, Z.; McHugh, E. A.; Algozeeb, W. A.; Yakobson, B. I.; Tour, J. M. Flash Graphene Morphologies. *ACS Nano* **2020**, *14*, 13691–13699.

20. Chen, W.; Wang, Z.; Bets, K. V.; Luong, D. X.; Ren, M.; Stanford, M. G.; McHugh, E. A.; Algozeeb, W. A.; Guo, H.; Gao, G.; Deng, B.; Chen, J.; Li, J. T.; Carsten, W. T.; Yakobson, B. I.; Tour, J. M. Millisecond Conversion of Metastable 2D Materials by Flash Joule Heating. *ACS Nano* **2021**, *15*, 1282–1290.

21. Chen, W.; Li, J. T.; Wang, Z.; Algozeeb, W. A.; Luong, D. X.; Kittrell, C.; McHugh, E. A.; Advincula, P. A.; Wyss, K. M.; Beckham, J. L.; Stanford, M. G.; Jiang, B.; Tour, J. M. Ultrafast and Controllable Phase Evolution by Flash Joule Heating. *ACS Nano* **2021**, *15*, 11158–11167.

22. Deng, B.; Wang, Z.; Chen, W.; Li, J. T.; Luong, D. X.; Carter, R. A.; Gao, G.; Yakobson, B. I.; Zhao, Y.; Tour, J. M. Phase Controlled Synthesis of Transition Metal Carbide Nanocrystals by Ultrafast Flash Joule Heating. *Nat. Commun.* **2022** *13*, 1–10.

23. Zhu, S.; Zhang, F.; Lu, H. G.; Sheng, J.; Wang, L.; Li, S. D.; Han, G.; Li, Y. Flash Nitrogen-Doped Graphene for High-Rate Supercapacitors. *ACS Mater. Lett.* **2022**, *4*, 1863–1871.

24. Eddy, L.; Luong, D. X.; Beckham, J. L.; Wyss, K. M.; Cooksey, T. J.; Scotland, P.; Choi, C. H.; Chen, W.; Advincula, P. A.; Zhang, Z.; Mancevski, V.; Kittrell, C.; Han, Y.; Tour, J. M. Automated Laboratory Kilogram-Scale Graphene Production from Coal. *Small Methods* **2024**, *8*, 2301144

25. Eddy, L.; Xu, S.; Liu, C.; Scotland, P.; Chen, W.; Beckham, J. L.; Damasceno, B.; Hun Choi, C.; Silva, K.; Lathem, A.; Han, Y.; Zhang, X.; Zhao, Y.; Tour, J. M. Electric Field Effects in Flash Joule Heating Synthesis. *J. Am. Chem. Soc.* **2024**, *146*, 16010–16019.

26. Dresselhaus, M. S.; Jorio, A.; Souza Filho, A. G.; Saito, R. Defect Characterization in Graphene and Carbon Nanotubes Using Raman Spectroscopy. *Philos. Trans. R. Soc., A* **2010**, *368*, 5355–5377.

27. Malard, L. M.; Pimenta, M. A.; Dresselhaus, G.; Dresselhaus, M. S. Raman Spectroscopy in Graphene. *Phys. Rep.* **2009**, *473*, 51–87.

28. Beckham, J. L.; Wyss, K. M.; Xie, Y.; McHugh, E. A.; Li, J. T.; Advincula, P. A.; Chen, W.; Lin, J.; Tour, J. M. Machine Learning Guided Synthesis of Flash Graphene. *Adv. Mater.* **2022**, *34*, 2106506.

29. Kim, K. K.; Lee, H. S.; Lee, Y. H. Synthesis of Hexagonal Boron Nitride Heterostructures for 2D van Der Waals Electronics. *Chem. Soc. Rev.* **2018**, *47*, 6342.

30. Wei, D.; Liu, Y.; Wang, Y.; Zhang, H.; Huang, L.; Yu, G. Synthesis of N-Doped Graphene by Chemical Vapor Deposition and Its Electrical Properties. *Nano Lett.* **2009**, *9*, 1752–1758.

31. Peng, W.; Liu, J.; Liu, X.; Wang, L.; Yin, L.; Tan, H.; Hou, F.; Liang, J. Facilitating Two-Electron Oxygen Reduction with Pyrrolic Nitrogen Sites for Electrochemical Hydrogen Peroxide Production. *Nat. Commun.* **2023** *14*, 1–11.

32. Chen, P.; Wang, L. K.; Wang, G.; Gao, M. R.; Ge, J.; Yuan, W. J.; Shen, Y. H.; Xie, A. J.; Yu, S. H. Nitrogen-Doped Nanoporous Carbon Nanosheets Derived from Plant Biomass: An Efficient Catalyst for Oxygen Reduction Reaction. *Energy Environ. Sci.* **2014**, *7*, 4095–4103

33. Ren, M.; Zhang, T.; Wang, Y.; Jia, Z.; Cai, J. A Highly Pyridinic N-Doped Carbon from Macroalgae with Multifunctional Use toward CO_2 Capture and Electrochemical Applications. *J. Mater. Sci.* **2019**, *54*, 1606–1615.

34. Chen, W. T.; Dutta, D.; Hung, Y. H.; Sin, Y. Y.; He, S. M.; Chang, J. K.; Su, C. Y. Designed Catalytic Protocol for Enhancing Hydrogen Evolution Reaction Performance of P, N-Co-Doped Graphene: The Correlation of Manipulating the Dopant Allocations and Heteroatomic Structure. *J. Phys. Chem. C* **2020**, *124*, 25701–25711.

35. Langer, R.; Błoński, P.; Hofer, C.; Lazar, P.; Mustonen, K.; Meyer, J. C.; Susi, T.; Otyepka, M. Tailoring Electronic and Magnetic Properties of Graphene by Phosphorus Doping. *ACS Appl. Mater. Interfaces* **2020**, *12*, 34074–34085.

36. Qian, J.; Wu, F.; Ye, Y.; Zhang, M.; Huang, Y.; Xing, Y.; Qu, W.; Li, L.; Chen, R. Boosting Fast Sodium Storage of a Large-Scalable Carbon Anode with an Ultralong Cycle Life. *Adv. Energy Mater.* **2018**, *8*, 1703159.

37. Yang, X.; Zhang, R. Y.; Zhao, J.; Wei, Z. X.; Wang, D. X.; Bie, X. F.; Gao, Y.; Wang, J.; Du, F.; Chen, G. Amorphous Tin-Based Composite Oxide: A High-Rate and Ultralong-Life Sodium-Ion-Storage Material. *Adv. Energy Mater.* **2018**, *8*, 1701827.

38. Wyss, K. M.; Silva, K. J.; Bets, K. V.; Algozeeb, W. A.; Kittrell, C.; Teng, C. H.; Choi, C. H.; Chen, W.; Beckham, J. L.; Yakobson, B. I.; Tour, J. M. Synthesis of Clean Hydrogen Gas from Waste Plastic at Zero Net Cost. *Adv. Mater.* **2023**, *35*, 2306763, 1-11.

39. Raymond, M. J.; Slater, C. S.; Savelski, M. J. LCA Approach to the Analysis of Solvent Waste Issues in the Pharmaceutical Industry. *Green Chem.* **2010**, *12*, 1826-1834

40. Jacquemin, L.; Pontalier, P. Y.; Sablayrolles, C. Life Cycle Assessment (LCA) Applied to the Process Industry: A Review. *Int. J. Life Cycle Assess.* **2012**, *17*, 1028–1041

41. Kyriaki, E.; Konstantinidou, C.; Giama, E.; Papadopoulos, A. M. Life Cycle Analysis (LCA) and Life Cycle Cost Analysis (LCCA) of Phase Change Materials (PCM) for Thermal Applications: A Review. *Int. J. Energy Res.* **2018**, *42*, 3068–3077.

42. Advincula, P. A.; Meng, W.; Eddy, L. J.; Beckham, J. L.; Siqueira, I. R.; Xuan Luong, D.; Chen, W.; Pasquali, M.; Nagarajaiah, S.; Tour, J. M.; Advincula, P. A.; Eddy, L. J.; Beckham, J. L.; Luong, D. X.; Chen, W.; Pasquali, M.; Tour, J. M.; Meng, W.; Nagarajaiah, S. Ultra-High Loading of Coal-Derived Flash Graphene Additives in Epoxy Composites. *Macromol. Mater. Eng.* **2023**, *308*, 2200640 (1-10).

TOC Graphic